ADVANCED MATERIALS
www.advmat.de

Check for updates

Large-Scale $Hf_{0.5}Zr_{0.5}O_2$ Membranes with Robust Ferroelectricity

Hai Zhong, Mingqiang Li, Qinghua Zhang, Lihong Yang, Ri He, Fang Liu, Zhuohui Liu, Ge Li, Qinchao Sun, Donggang Xie, Fanqi Meng, Qiang Li, Meng He, Er-jia Guo, Can Wang, Zhicheng Zhong, Xinqiang Wang, Lin Gu, Guozhen Yang, Kuijuan Jin, Peng Gao,* and Chen Ge**

Hafnia-based compounds have considerable potential for use in nanoelectronics due to their compatibility with complementary metal–oxide–semiconductor devices and robust ferroelectricity at nanoscale sizes. However, the unexpected ferroelectricity in this class of compounds often remains elusive due to the polymorphic nature of hafnia, as well as the lack of suitable methods for the characterization of the mixed/complex phases in hafnia thin films. Herein, the preparation of centimeter-scale, crack-free, freestanding $Hf_{0.5}Zr_{0.5}O_2$ (HZO) nanomembranes that are well suited for investigating the local crystallographic phases, orientations, and grain boundaries at both the microscopic and mesoscopic scales is reported. Atomic-level imaging of the plan-view crystallographic patterns shows that more than 80% of the grains are the ferroelectric orthorhombic phase, and that the mean equivalent diameter of these grains is about 12.1 nm, with values ranging from 4 to 50 nm. Moreover, the ferroelectric orthorhombic phase is stable in substrate-free HZO membranes, indicating that strain from the substrate is not responsible for maintaining the polar phase. It is also demonstrated that HZO capacitors prepared on flexible substrates are highly uniform, stable, and robust. These freestanding membranes provide a viable platform for the exploration of HZO polymorphic films with complex structures and pave the way to flexible nanoelectronics.

1. Introduction

Hafnia-based compounds have attracted considerable research interest since their unconventional ferroelectricity was discovered in 2011.[1] Their complementary metal–oxide–semiconductor (CMOS) compatibility[2] and robust nanoscale ferroelectricity[3,4] strongly suggest that hafnia-based ferroelectrics are promising candidates for the next generation of low-power nonvolatile memories, logic devices,[5] and other nanoelectronics.[6–9] Hafnia-based compounds usually are polymorphic in nature, and more than ten stable and metastable phases have been identified in such compounds in experimental and computational works.[10–13] The unconventional ferroelectric properties of hafnia are generally believed to originate from a non-centrosymmetric orthorhombic metastable phase (o-phase, $Pca2_1$).[1,11,14] However, the stabilization mechanism of this metastable ferroelectric phase remains controversial. Various

H. Zhong, Q. Zhang, L. Yang, Z. Liu, G. Li, Q. Sun, D. Xie, F. Meng, M. He, E.-j. Guo, C. Wang, L. Gu, G. Yang, K. Jin, C. Ge
Beijing National Laboratory for Condensed Matter Physics
Institute of Physics
Chinese Academy of Sciences
Beijing 100190, China
E-mail: kjjin@iphy.ac.cn; gechen@iphy.ac.cn

H. Zhong, C. Wang, Z. Zhong, L. Gu, K. Jin, C. Ge
University of Chinese Academy of Sciences
Beijing 100049, China

M. Li, P. Gao
Electron microscopy laboratory and International Center for Quantum Materials
School of Physics
Peking University
Beijing 100871, China
E-mail: p-gao@pku.edu.cn

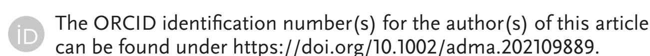
The ORCID identification number(s) for the author(s) of this article can be found under https://doi.org/10.1002/adma.202109889.

DOI: 10.1002/adma.202109889

R. He, Z. Zhong
Key Laboratory of Magnetic Materials Devices & Zhejiang Province Key Laboratory of Magnetic Materials and Application Technology
Ningbo Institute of Materials Technology and Engineering
Chinese Academy of Sciences
Ningbo 315201, China

F. Liu, X. Wang
State Key Laboratory for Mesoscopic Physics and Frontiers Science Center for Nano-optoelectronics
School of Physics
Peking University
Beijing 100871, China

Q. Sun, Q. Li
College of Physics
University-Industry Joint Center for Ocean Observation and Broadband Communication
State Key Laboratory of Bio-Fibers and Eco-Textiles Qingdao University
Qingdao 266071, China

X. Wang, P. Gao
Collaborative Innovation Centre of Quantum Matter
Beijing 100871, China

© 2022 Wiley-VCH GmbH

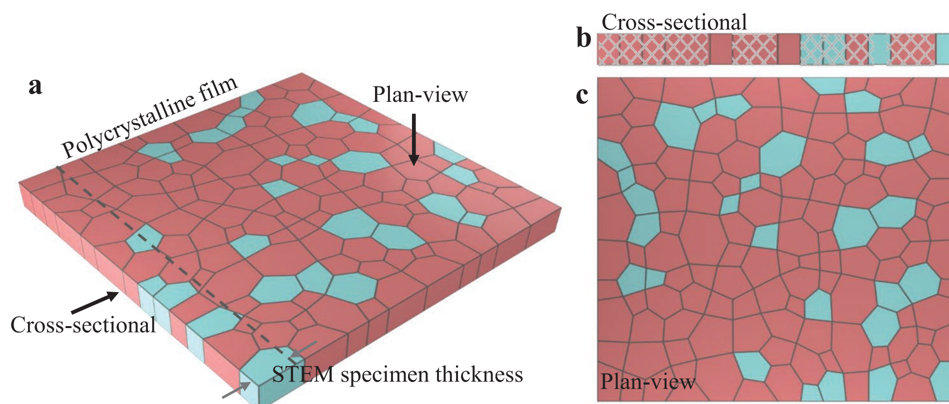

Figure 1. Comparison between cross-sectional and plan-view characterization of epitaxial polycrystalline films. a) Schematic of a polycrystalline film with nanosized grains. The different colored areas represent different crystal structures, such as the monoclinic phase and orthorhombic phase in hafnia-based materials. The dashed line indicates a typical sample cross section with a thickness of tens of nanometers imaged with STEM. b) Atomic-level information on most of the cross-sectional area (grid covered) cannot be obtained from polycrystalline samples because the atomic columns of different grains are misplaced or not aligned with the imaging direction. c) Atomic-level information for most grains and even grain boundaries can be obtained from plan-view imaging since polycrystalline films usually have an epitaxial orientation and a thickness ranging from several nanometers to tens of nanometers.

possible factors such as strain,[15–17] doping,[18,19] oxygen vacancies,[20,21] and surface and grain boundary energies[22] have been put forward as contributing to the stability of the ferroelectric o-phase. The uncertainty surrounding the stabilization mechanism has primarily arisen from the polymorphic nature of hafnia films and the challenges associated with the characterization of mixed/complex phases in thin films.[23]

Cross-sectional scanning transmission electron microscopy (STEM) is commonly used to investigate the complex structure of hafnia-based films,[24,25] while this method only provides structural information of a small fraction of the grains and grain boundaries in polycrystalline films with nanosized grains (**Figure 1**). On the other hand, plan-view imaging provides more comprehensive structural information and is better suited for characterizing hafnia-based films. There have been some efforts through using plan-view characterization methods, such as electron back-scattering diffraction[26] and X-ray absorption spectroscopy (XAS),[27] to characterize hafnia-base films. Wei et al. thinned the film substrate to take plan-view transmission electron microscopy (TEM) images and investigated the average grain size.[12] However, atomic-level structural imaging has not yet been realized due to interference effects from the substrates.

The advent of freestanding crystalline oxide membranes[28–30] presents new opportunities to address challenges in plan-view characterization of thin films. By selectively etching a buffer layer, complex oxide membranes are released from the substrate. The released membranes can be directly transferred to TEM grids, providing an ideal platform to investigate the structure of oxide membranes from plan view.[29] Following this route, atomic-level imaging of the different phases, phase boundaries, grain sizes, phase orientations, and relative phase proportions in hafnia membranes can thus be realized on a large scale. Moreover, this freestanding membrane approach also provides an opportunity to design a system without epitaxial strain[31,32] and can provide new insights into the stabilization of the metastable ferroelectric phase of hafnia-based films.

Herein, we report centimeter-scale, crack-free, freestanding $Hf_{0.5}Zr_{0.5}O_2$ membranes with robust ferroelectricity for the first time. Atomic-level images of the plan-view crystallographic patterns were obtained, and the grain radii, phase distributions, grain orientations, boundaries, subgrain domain walls, and interphase boundaries were analyzed. Studies of the substrate-free membranes showed that the ferroelectric orthorhombic structure evolved from the compressively strained as-grown structure. This new perspective provides a foundation for the study of the complex structure of polymorphic HZO films at both the microscopic (atomic) and mesoscopic (grain structures) scales. Furthermore, ferroelectric hysteresis measurements showed that the performance of the HZO capacitors prepared on flexible substrates was highly uniform, stable, and robust.

2. Results and Discussion

We synthesized HZO/$La_{0.8}Sr_{0.2}MnO_3$ (LSMO) heterostructures on single crystal SrTiO3 (STO) substrates via pulsed-laser deposition (PLD). After fully dissolving the sacrificial LSMO layer in acid etchant, the HZO film was released from the substrate and then readily transferred to other substrates (**Figure 2**a–c, further details in the Experimental Section). The centimeter-scale (1×1 cm^2) freestanding HZO (4–10 nm) membranes were easily released from the STO substrates by floating the film on a water surface. The membranes then were transferred onto oxidized silicon substrates, commercial transparent poly(ethylene terephthalate) (PET) sheets, or holey carbon TEM grids (Figure 2d,e; Figure S1, Supporting Information). Using both optical microscopy and atomic force microscopy (AFM), we characterized the topography of the resulting freestanding membranes and noted that the centimeter-scale films were laterally free of cracks and had a low surface roughness of about 0.20 nm (Figure S2, Supporting Information). Unlike common problems, such as crack formation and folding, seen in the

© 2022 Wiley-VCH GmbH

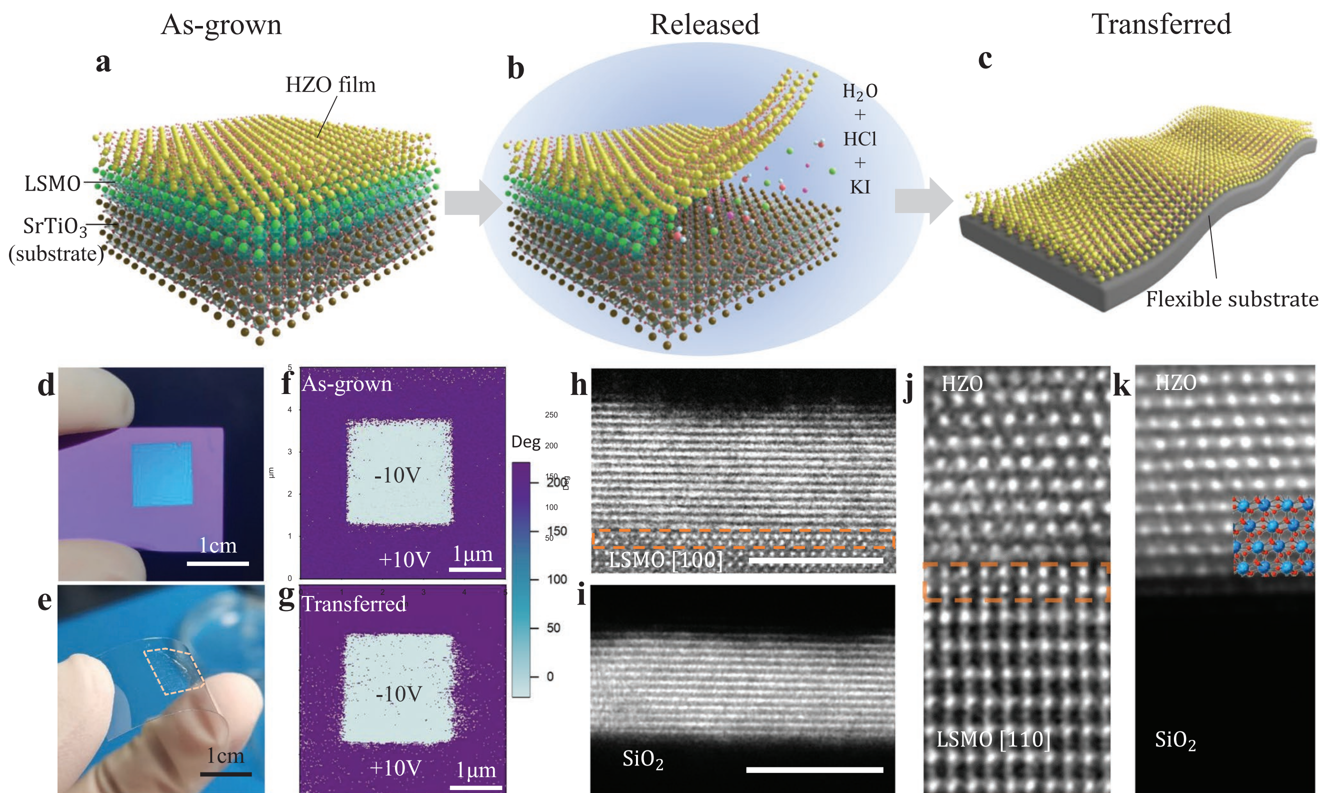

Figure 2. Preparation and transfer of freestanding HZO films. a) Schematic of a HZO film with a LSMO buffer layer. b) The sacrificial LSMO layer is dissolved in etchant to release the top HZO film. c) New heterostructures and interfaces are formed when the freestanding film is transferred onto the desired substrate. d,e) Photograph of a 10 nm-thick freestanding HZO film transferred to an oxidized silicon substrate (d) and to a PET flexible substrate (e). f,g) Out-of-plane PFM phase of the as-grown 10nm-thick HZO film on LSMO/STO (f) and the 10 nm-thick HZO membrane transferred to Pt/SiO_2 (g). Scale bar: 1 µm. h,i) Cross-sectional HAADF images of HZO/LSMO from the LSMO [100] direction (h) and a freestanding HZO membrane transferred to an oxidized silicon substrate (i). Scale bar: 5 nm. j,k) Magnified cross-sectional HAADF images of HZO/LSMO from the LSMO [110] direction (j) and a freestanding HZO membrane transferred to an oxidized silicon substrate (k), together with schematic crystal structures.

preparation of most freestanding oxide membranes, the large area HZO nanomembranes were crack-free, which is important for their use in practical applications. Moreover, piezoresponse force microscopy (PFM) (Figure 2f,g; Figure S3, Supporting Information) and polarization–electric field (*P–E*) loop measurements (Figure S4, Supporting Information) showed that the ferroelectricity of the HZO films was well-preserved after transfer.

We also confirmed the quality of HZO film before and after transfer using cross-sectional STEM. The interface between the LSMO and HZO layers was sharp and clear in the as-grown HZO (5 nm)/LSMO heterostructure (Figure 2h). Although the Hf/Zr atomic columns were not well resolved in the [100] direction of the LSMO, the clear stripes in the images indicated that the grown HZO film was good quality. Atomically resolved images of the epitaxial heterostructure showed the films grew in the LSMO [110] direction (Figure 2j). Figure 2i,k shows that the structure of the HZO (4 nm) film transferred to a Si substrate was very similar to that of the as-grown film.

X-ray diffraction (XRD) measurements were used to confirm the structure of the HZO films. In the θ–2θ patterns of the as-grown HZO films, the main Bragg peak appeared at ≈30° (**Figure 3**a). This value was lower than that reported for the polar o-phase (111) reflection,[33] indicating that a compressive in-plane strain was present in our HZO films. The polar figure measurements and 2θ scans for all 13 reflections (Figure S5, Supporting Information) of the 10 nm-thick HZO sample indicated that the *d*-spacing values were $d_{11-1} = d_{1-11} = d_{-111} = 2.94$ Å $< d_{111} = 2.97$ Å, revealing that the as-grown film was likely a rhombohedral structure.[12] Laue oscillations were clearly visible in both the 10 nm and 5 nm HZO films, suggesting the samples here highly crystalline and the interfaces were sharp. In addition, the (002) peak of monoclinic HZO (m-HZO, $P2_1/c$) was barely visible in the diffraction pattern of the 10 nm HZO film and was invisible in the diffraction pattern of the 5 nm HZO film, suggesting that the (111) ferroelectric phase was the primary phase in our as-grown samples.

In the diffraction pattern of the HZO film transferred to a Si (100) substrate, the main peaks slightly shifted to the right due to the relaxation of the compressive in-plane strain. We calculated the (111)-spacing, d_{111}, in the out-of-plane direction for all prepared HZO samples (Figure 3b). Using the 5 nm-thick HZO membrane as an example, the lattice constant decreased from 2.978 to 2.954 Å after the film was transferred due to the loss of the substrate clamping effect, corresponding to ≈0.8% stress relief. It was crucial to confirm the specific structure of the transferred HZO films. As such, pole figure measurements were performed around the (111) peak of a transferred

© 2022 Wiley-VCH GmbH

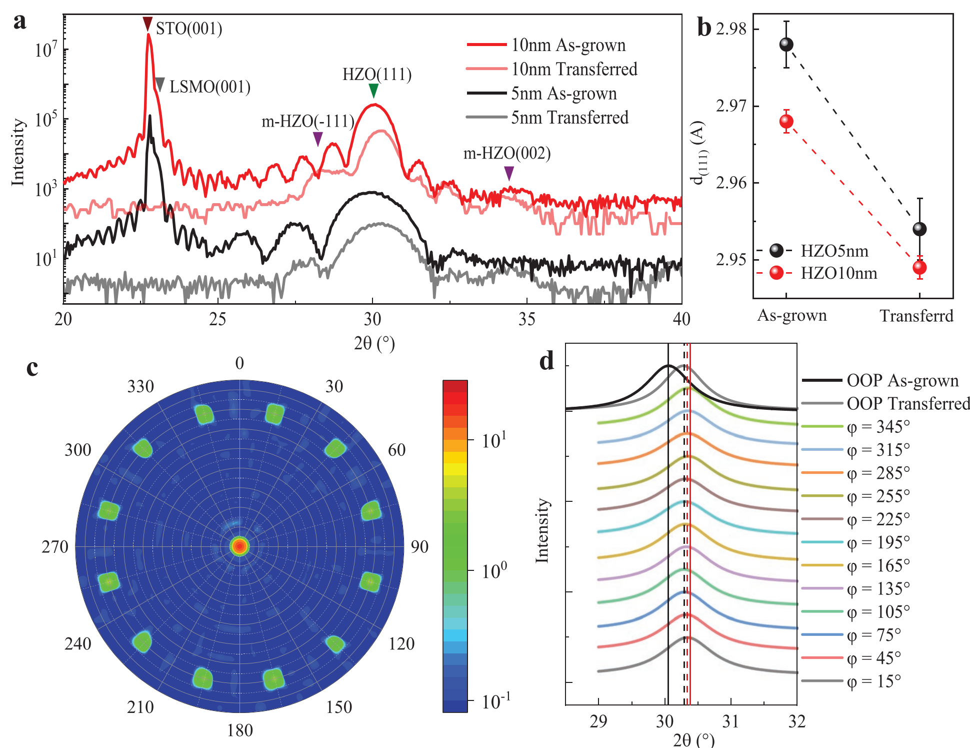

Figure 3. X-ray diffraction measurements of the as-grown HZO films and HZO membrane transferred to silicon. a) θ–2θ scans of the as-grown HZO films on $La_{0.8}Sr_{0.2}MnO_3/SrTiO_3$ substrates and the transferred HZO films on Si (001) substrates. b) Lattice constants, d_{111}, before and after transfer of the HZO films, calculated from (a). c) Pole figure around the (111) peak of a 10 nm HZO film at $2\theta = 30.29°$. The radial direction represents χ and ranges between 0° and 90°, while the azimuthal direction represents φ and ranges from 0°–360°. The logarithmic color scale represents intensity. d) 2θ scans of the 13 peaks in the pole figure. The black solid line and black dashed line indicate the out-of-plane (111) reflection positions of the as-grown and transferred films, respectively. The red solid line and red dashed line indicate the (11–1) (1–11) (–111) reflection positions of the as-grown and transferred films, respectively. All the lines in (d) are drawn from a Lorentz simulation of raw data.

10 nm HZO film. Similar to the as-grown film, 12 reflections corresponding to the (–111), (11–1), and (1–11) planes were found at $\chi \approx 71°$ (Figure 3c). We also performed 2θ scans for all 13 reflections, as shown in Figure 3d. These scans clearly showed that the out-of-plane (111) reflection shifted to higher angles, highlighted by the solid black line and dotted black lines in the figure, but the other 12 reflections showed a slight shift to lower angles, as shown by the solid red line and dashed red line, compared with the reflections of the as-grown sample. All reflections appeared at almost the same angle, such that $d_{11-1} = d_{1-11} = d_{-111} = 2.944$ Å $\approx d_{111} = 2.949$ Å. The 2θ values of the peaks for the transferred film were in good agreement with that of the (111) reflections commonly reported for the ferroelectric o-phase in HZO.[33] Thus, these results clearly indicated that ferroelectric o-HZO was present in our freestanding membranes from the compressively strained as-grown HZO films. It should be noted that there may be additional factors that influenced the film structure during transfer. In view of the important role oxygen content plays in the phase transitions of HZO,[34] a slight change in the oxygen content of the HZO layer may occur during removal of LSMO, which could affect the phase structure, and future experiments would be needed to further investigate this potential effect.

To obtain atomic-level plan-view images, we transferred the freestanding HZO membranes onto holey carbon TEM grids (Figure S1d, Supporting Information). As shown in **Figure 4**a, the polymorphic structure of the HZO thin films was visible, with grain sizes ranging from a few to tens of nanometers. Atomic resolution was achieved in most regions, although misalignment of the lattice tilts resulted in lower resolution in some regions.[29] Each individual grain was either a single crystal or polycrystalline, showing a certain degree of randomness. Various crystal structures were visible, and the dominant structure is shown in Figure 4b. By fitting with a standard structure model, we verified that the dominant structure corresponded to the o-HZO [111] direction, and the arrow denotes the [11–2] direction, which showed a striped structure of a different width. The regions of o [010] and m [–111] phases are also marked in Figure 4a, and their crystal structures are shown in Figure 4c,d, respectively. In addition, we found a small amount of m [100] and m/o [001] structures in other areas of the sample, as shown in Figure 4e,f. The results of the TEM image analysis were consistent with the XRD results, in which the o-(111) reflections were much stronger than the other orientations. As for the structure in Figure 4f, we could not distinguish whether it was an m [001] or o [001] phase from the plan-view atomic configuration, and the structure may have even contained a coherent interface between these two phases.[24] The atomic models of o-/m-phase HZO and the corresponding fast Fourier transform patterns of all the phases are shown in Figure S6 in the Supporting Information. Among these phases, only the o-HZO [111] contributes to the out-of-plane ferroelectricity of the thin films.

© 2022 Wiley-VCH GmbH

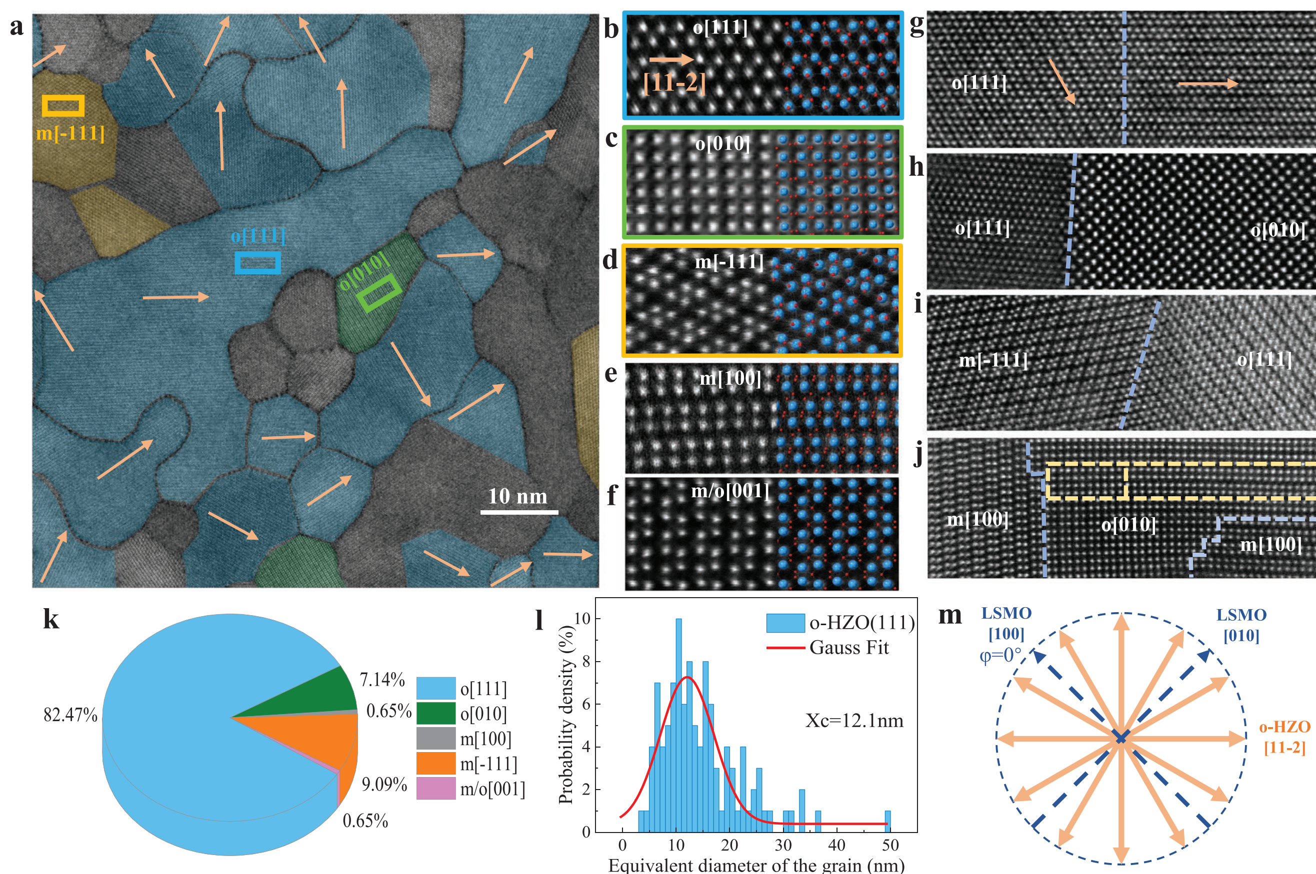

Figure 4. Crystallographic phases and orientations of HZO membranes from the plan-view. a) Representative large-scale image and atomically resolved plan view of the 10 nm HZO membrane. b–f) Magnified regions in a showing various crystal phases and orientations of the HZO structure. g–j) Two types of ferroelectric domain walls (g,h), and two types of coherent phase boundaries (i,j) observed in HZO membranes. k) Proportions of each phase and orientation. We only counted grains that were clearly recognizable. l) Grain-size distribution of the o-(111) phase, where Xc is the median thickness value. m) Statistical analysis of the o-HZO [11–2] direction relative to the LSMO buffer layer. The orange arrows marked in (a), (b), and (g) indicate the direction of the stripes, that is, the [11–2] direction of o-HZO.

In addition, many domain wall configurations and coherent phase boundaries were observed in the atomic-level images and plan-view crystallographic patterns. Two ferroelectric domain wall configurations with different angles are shown in Figure 4g,h, corresponding to ≈54° (or 126°) and ≈48° (or 132°), respectively. This was unexpected because domain walls with angles of 90° and 180° only were predicted and observed in previous studies of hafnia-based compounds.[35,36] Figure 4i,j shows two types of coherent interfaces between o-HZO and m-HZO phases, and the coherent interface shown in Figure 4i is reported for the first time. Phase transformation between the m-phase and o-phase most likely occurs at this coherent interface, which could be important for exploring the origins of wake-up and fatigue processes.[37] The yellow rectangle in Figure 4j shows the evolution of the m-phase into the o-phase, which is considered to be a manifestation of the distortion of the tetragonal phase (t-phase) into the o-phase and m-phase. In addition, a monoclinic-like major distortion layer was present between two major distortion units with orthorhombic-like structures, suggesting that substitution of a monoclinic-like distorted layer into an orthorhombic lattice resulted in an antiphase-like boundary in the orthorhombic phase.[24]

Next, we performed quantitative analysis of the different regions in the plan-view images. First, we counted the proportions of each phase and each orientation. More than 150 atomically resolved domains were counted, of which the o [111] and o [010] phases accounted for 82.47% and 7.14% of the domains, respectively. The total proportion of the m-phase in each orientation was about 10%, indicating that the o-phase was the dominant phase in our HZO films. Plan-view mode can probably allow the imaging of larger areas, and this could allow accurately quantifying the evolution of phases with thickness. We also calculated the size of approximately 110 o-HZO [111] domains and found that the mean equivalent diameter of the orthorhombic grains was about 12.1 nm, with a standard deviation of ≈10 nm, and all values of the diameters ranged from 4 to 50 nm. The domain areas varied from 10 nm^2 to larger than 1000 nm^2, with an average value of 83.7 nm^2 (Figure S7, Supporting Information). Information on the explicit grain-size distributions and grain boundary configurations in HZO films will be helpful for improving a previously reported free energy model and for understanding the stabilization mechanism of the ferroelectric o-phase.[22] This method of using freestanding thin films to obtain plan-views enables the easy investigation of

 © 2022 Wiley-VCH GmbH

the microstructural evolution in HZO films at the microscopic and mesoscopic scales, and this structural information is of broad interest in application-driven research such as the variability of ferroelectric field-effect transistors (FeFETs).[38]

By analyzing the $[11\text{–}2]_{HZO}$ direction relative to the LSMO buffer layer in 67 o-HZO (111) domains (Figure 4a; Figure S8, Supporting Information), we found that there were $[11\text{–}2]_{HZO}$ stripes with 12 in-plane directions. The angle between the $[11\text{–}2]_{HZO}$ stripes and $[100]_{LSMO}$ obeyed $\varphi = 15° + n \times 30°$ (n = 0, 1, 2 ... 11; where the $\varphi = 0°$ direction was defined as the $[100]_{LSMO}$ direction), as shown in Figure 4m. In view of the fourfold symmetry of LSMO (001) buffer layer, three epitaxial relationships of o-HZO grown on LSMO (001) were deduced. They are [11–2]HZO(111)//[110]LSMO(001) and [2–20]HZO(111)//[1–10]LSMO(001); [20–2]HZO(111)//[110]LSMO(001) and [1–21]HZO(111)//[1–10]LSMO(001); [02–2]HZO(111)//[110]LSMO(001) and [2–1–1]HZO(111)//[1–10]LSMO(001), as shown in Figure S9 in the Supporting Information. It should be noted that the three epitaxial relationships are the same for a cubic or rhombohedral structure, but are different for an orthorhombic structure. The complicated epitaxial relationships indicated that there should be more domain orientations and domain wall configurations in the prepared films. For example, the 54° (or 126°) domain wall in Figure 4g corresponded to two (111)-oriented domains with a relative angle of 60° (or 120°).

Factors that potentially stabilize the ferroelectric orthorhombic phase in HZO films have been discussed in a wide range of literature, but the roles of these factors remain controversial. Strain from the substrate is generally considered one of the most important factors for promoting and stabilizing the ferroelectric o-phase.[15,16,39] However, our results demonstrate that although the in-plane strain from the buffer layer has a crucial impact on the stabilization of the ferroelectric o-HZO during the film growth process,[40] the strain is not responsible for maintaining the metastable phase once it has formed. Materlik et al.[11] and Park et al.[22] have developed models for the surface and grain boundary energies to explain the stabilization of o-HZO. The ferroelectric o-phase in hafnia-based materials is usually found in thin films with small grain sizes, and as such, the contribution of the grain boundary energy to the total free energy of the film is significant in thin films with abundant grain boundaries. The surface and grain boundary energies should play an important role in stabilizing and maintaining the ferroelectric o-phase in nanoscale HZO films. The detailed information on the grain sizes and boundaries obtained by atomic-level plan-view imaging, such as the surface orientations and atomic configurations at grain boundaries, may be important for accurately calculating the relative contributions to the free energy.

With increasing demand for a myriad of emerging wearable applications in recent years, flexible electronic devices have gained attention for their remarkable softness, exceptional versatility, and human-friendly interfaces.[41] Previous studies showed that HZO thin films directly grown on flexible mica substrates had robust ferroelectricity and promising application potential in flexible electronics.[42–45] The distinct advantage of our freestanding HZO membranes is that they can be easily transferred to almost any substrate to fabricate electronic devices, including substrates that cannot be annealed at high temperatures. Here we transferred the HZO capacitors onto mica as an example to demonstrate the robust ferroelectricity of our freestanding HZO membranes in flexible electronic devices.

A freestanding HZO membrane with Pt electrodes was transferred to a Pt/mica substrate to fabricate HZO capacitors. The performances of the flat and bent HZO capacitors were characterized at room temperature to explore their bending reliability and flexibility (**Figure 5**a). None of the measurements required a wake-up procedure. Figure 5b shows the *P*–E hysteresis loops of the same device after different numbers of bending cycles. The detailed loops under different voltages are shown in Figure S10 in the Supporting Information. All hysteresis loops showed negligible differences in parameters, and the positive remanent polarization (+Pr), negative remanent polarization (–Pr), positive coercive field (+Ec), and negative coercive field (–Ec) were about 22 μC cm^{-2}, –21 μC cm^{-2}, 2.87 MV cm^{-1}, and –3.35 MV cm^{-1}, respectively. These values were in good agreement with those reported for HZO films on LSMO/STO substrates,[12,46] indicating that the HZO retained its good ferroelectric properties in different bent states. The applied bending strains were estimated using the equation $S = D/2R$,[47] where S is the strain induced on the surface, D is the thickness of the substrate (≈10 μm), and R is the bent radius of the film. The bending strain at a radius of 1 cm was as low as ≈0.05%, and its influence on the HZO membrane properties was negligible. Figure 5c shows the detailed parameters of the *P*–*E* loops measured of 20 devices under different bending states, and Figure 5d shows these parameters after 100, 500, 1000, and 2000 cycles of bending to a radius of 1 cm. All the parameter values were stable with decreasing bending radii and increasing numbers of bending cycles. We further performed *P*–*E* tests over a wide temperature range (100–400 K) to evaluate the reliability of the devices in harsh environments, such as in space (Figure 5e,f). Across the whole temperature range, the HZO capacitors showed significant ferroelectricity, but the Pr value increased slowly with increasing temperature, which was contrary to the temperature dependence seen in conventional ferroelectrics but in line with polarization switching behavior correlated to the thermally activated oxygen migration mechanism.[25] This observation reflects that the origins of the ferroelectric properties of hafnia-based materials are quite different from that of conventional perovskite ferroelectric materials. Overall, these results indicate that the ferroelectricity of our freestanding HZO membranes is robust under repeated mechanical flexing and in a wide range of temperatures.

Large-scale ultrathin films with stable ferroelectricity are highly desirable for practical applications. Previous works have used ferroelectric perovskite oxide membranes, such as $BaTiO_3$ and $BiFeO_3$, and 2D ferroelectrics, such as $CuInP_2S_6$ (CIPS)[48] and In_2Se_3,[49] to make flexible electronic devices. However, single crystalline perovskite oxide membranes usually have issues with folding and crack formation due to mechanical damage to the membrane when the supporting layers are removed and strain relaxation caused by lattice mismatch occurs.[50,51] 2D ferroelectrics also have weaker ferroelectricity and smaller membrane sizes compared to oxide ferroelectrics.[52] Here, we obtained centimeter-scale crack-free

© 2022 Wiley-VCH GmbH

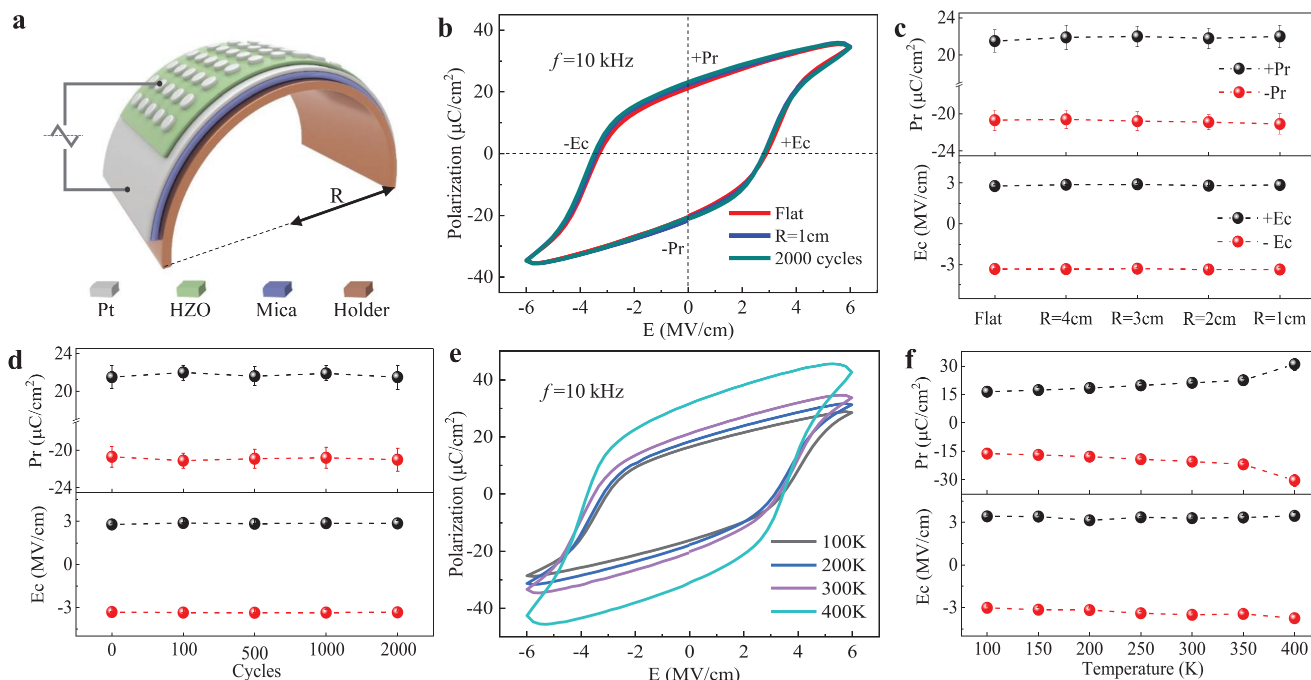

Figure 5. Ferroelectric properties of flexible HZO capacitors in different testing environments. a) Schematic diagram of flexible ferroelectric HZO capacitors. b) Polarization–electric field (*P–E*) hysteresis loops at 10 kHz. c,d) Variation of Pr (remanent polarization) and Ec (coercive field) of flexible HZO capacitors at different bending radii (c) and after multiple bending cycles (d). e) *P–E* hysteresis loops at different temperatures. f) Variation of Pr and Ec of flexible HZO capacitors at different temperatures.

nanomembranes with robust ferroelectricity, and such properties are unattainable in crystalline perovskite oxide membranes and 2D ferroelectrics (Table S1, Supporting Information). The disordered grain boundaries in nanograined films may have played an important role in strengthening the freestanding HZO membranes prepared here.[53] Our work indicates that introducing grain boundaries may be a solution to achieve centimeter-scale, crack-free, freestanding oxide membranes.

3. Conclusions

We have successfully fabricated centimeter-scale, freestanding HZO nanomembranes and confirmed their robust ferroelectricity. The transferred HZO membranes were composed primarily of the stable ferroelectric orthorhombic phase, indicating that the strain from the substrate was not necessary to maintain the polar phase. The results suggested that the surface and grain boundary energies likely played an important role in stabilizing the ferroelectric phase; however, other factors such as doping and oxygen vacancies still need to be studied further. By transferring the freestanding HZO membranes to TEM grids, the phases, orientations, size distributions, and boundaries of the grains were atomically characterized from plan-view, allowing for the epitaxial relationships and domain walls to be derived. Our work opens a new paradigm for exploring unconventional ferroelectricity in polymorphic HZO membranes using plan-view imaging. Moreover, we also demonstrated the good uniformity, stability, and robustness of HZO capacitors on flexible substrates. From a technological perspective, the large-scale, crack-free HZO nanomembranes could be transferred to other materials to fabricate nanoelectronic devices without compatibility issues related to annealing. Accordingly, these HZO membranes can be used to design various flexible ferroelectric devices including ferroelectric memories, negative capacitance FETs, and neuromorphic devices.

4. Experimental Section

Thin-Film Growth: HZO thin films with thicknesses of 5 or 10 nm and an LSMO buffer layer with a thickness of 20 nm were grown by pulsed laser deposition on STO (001) substrates. An XeCl excimer laser with a wavelength of 308 nm was used, and the imaged laser spot size was 4.0 mm^2. The LSMO layer and HZO layer were grown under oxygen pressures of 25 and 13 Pa, respectively. A growth temperature of 750 °C, a laser fluence of 1.25 J cm^{-2}, and a repetition rate of 2 Hz were employed to grow both layers. After deposition, the heterostructure was cooled down to room temperature at a rate of 10 °C min^{-1} under an oxygen pressure of 10 kPa.

HZO Membrane Fabrication: After growth, the HZO films were released from the STO substrate by selective etching of the sacrificial LSMO layer. The unclamped thin films were then removed from the substrate by slowly dipping the substrate in deionized water. It should be noted that the samples should be placed horizontally and immersed smoothly into the water. During this process, the deionized water will slowly infiltrate into the gap between the HZO film and the substrate, replacing the original etching solution. When done correctly, the released films floated on the water surface (Figure S1c, Supporting Information). A homemade copper wire loop was then used to catch the freestanding HZO membranes from the water surface. The films were held in place by a thin layer of water formed inside the metal loop. The released films were then moved to target substrates placed on a 95 °C hot plate. The water was allowed to evaporate, leaving HZO films on target substrates such as silicon, PET, a TEM grid (Figure 2d,e; Figure S1f, Supporting Information), and mica.

X-ray Structural Characterization: XRD measurements were performed using high-resolution X-ray diffractometer (Rigaku Smartlab) to

 © 2022 Wiley-VCH GmbH

characterize the structure and orientation of the films. The θ–2θ specular scans were carried out in a line focus of the incident beam mode with step width of 0.02°–0.05° to probe the lattice parameters. The pole figures were operated in a point focus of the incident beam mode, in which φ (azimuthal angle) and χ (tilt of the sample plane around the incident beam direction) are scanned while the detector is fixed at a particular Bragg reflection. The pole figures of as-grown and transferred HZO films were performed by using a X'Pert[3] MRD system and a Rigaku Smartlab system, respectively. Cu anode was used in the X-ray tube and the corresponding wavelength is 1.5406 Å.

AFM and PFM Measurement (Scanning Probe Microscopy): AFM and PFM measurements were performed using a commercial scanning probe microscope (Asylum Research MFP-3D). Oxford Inc. HQ-75 Au/Ti-coated Si probe tips were used in the AFM measurements and the imaging mode is tapping mode. Nanosensor PPP-EFM-10 Ir/Pt coated conductive tips were used for PFM imaging. Local hysteretic behaviors of the PFM phase and amplitude signals were collected in DART (dual A.C. resonance tracking) mode and the signals were recorded while the voltage was off. In both the hysteresis loop and PFM contrast mapping measurements, drive amplitudes applied on the tip were 1.5 Vac. During the domain writing, the switching voltage were ±10 V.

Hysteresis Measurement: Pt (50 nm) round electrodes with diameter 30 µm were deposited by a homemade magnetron sputtering system and patterned by standard microfabrication technology. The Pt/HZO/LSMO (as-grown) and Pt/HZO/Pt/ (transferred) capacitors were measured using a precision multiferroic analyzer (RADIANT Tec. Inc.). The *P–E* hysteresis loops were obtained via simple hysteresis mode, triangular pulses with frequency of 10 kHz were applied to reverse the polarization of ferroelectric HZO layer. In the *P–E* measurements under various temperatures, the samples were adhered to a copper plate and placed into a vacuum probe station (Lake Shore TTPX). Liquid nitrogen was used to cool the whole copper plate. Tungsten probes were used for all the *P–E* measurements.

Electron Microscopy: For cross-sectional microscopy, sample was prepared by using focused ion beam (FIB) milling. Cross-sectional lamellas were thinned down to 60 nm thick at an accelerating voltage of 30 kV with a decreasing current from the maximum 2.5 nA, followed by fine polish at an accelerating voltage of 2 kV with a small current of 40 pA. The atomic structures of the HZO and LSMO films was characterized using an ARM 200CF (JEOL, Tokyo, Japan) transmission electron microscope operated at 200 kV and equipped with double spherical aberration (Cs) correctors. High-angle annular dark-field (HAADF) images were acquired at acceptance angle of 90–370 mrad. For plan-view microscopy, the sample was prepared by transferring freestanding HZO membranes on a holey carbon TEM grid. The HAADF images in this work were obtained using probe Cs-corrected FEI Titan 60–300 (Titan Themis G2 in Electron Microscopy Laboratory of Peking University) operated at 300 kV. The convergence semiangle is 30 mrad, and the angular range of the HAADF detector is from 39 to 200 mrad.

Supporting Information

Supporting Information is available from the Wiley Online Library or from the author.

Acknowledgements

This work was supported by the National Key R&D Program of China (Nos. 2017YFA0303604 and 2019YFA0308500), the Youth Innovation Promotion Association of CAS (No. 2018008), and the National Natural Science Foundation of China (Nos. 12074416, 11674385, 11721404, 22179066, 52072400, and 52025025).

Conflict of Interest

The authors declare no conflict of interest.

Author Contributions

H.Z. and M.L. contributed equally to this work. The sample preparation, the device fabrication, and the device measurement were done by H.Z. with support from G.L. XRD measurements were performed by L.Y., X.W., F.L., and H.Z. PFM measurements were carried out by Q.S. and Z.L. Plan-view STEM measurements were performed by M.L. and P.G. Cross-sectional STEM measurements were done by Q.Z., F.M., and L.G. H.Z., C.G., M.L., Q.Z., P.G., and L.G. analyzed the experimental data. C.G. and H.Z. wrote the manuscript with inputs from M.L. and P.G. All authors participated in the discussion of manuscript. C.G. initiated the research. C.G. and K.J. supervised the project.

Data Availability Statement

The data that support the findings of this study are available from the corresponding author upon reasonable request.

Keywords

ferroelectric domains, ferroelectric phases, flexible ferroelectrics, freestanding membranes, $Hf_{0.5}Zr_{0.5}O_2$

Received: December 5, 2021
Revised: April 5, 2022
Published online:

[1] T. S. Böscke, J. Müller, D. Bräuhaus, U. Schröder, U. Böttger, *Appl. Phys. Lett.* **2011**, *99*, 102903.
[2] M. H. Park, Y. H. Lee, T. Mikolajick, U. Schroeder, C. S. Hwang, *MRS Commun.* **2018**, *8*, 795.
[3] S. S. Cheema, D. Kwon, N. Shanker, R. Dos Reis, S.-L. Hsu, J. Xiao, H. Zhang, R. Wagner, A. Datar, M. R. Mccarter, C. R. Serrao, A. K. Yadav, G. Karbasian, C.-H. Hsu, A. J. Tan, L.i-C. Wang, V. Thakare, X. Zhang, A. Mehta, E. Karapetrova, R. V. Chopdekar, P. Shafer, E. Arenholz, C. Hu, R. Proksch, R. Ramesh, J. Ciston, S. Salahuddin, *Nature* **2020**, *580*, 478.
[4] H.-J. Lee, M. Lee, K. Lee, J. Jo, H. Yang, Y. Kim, S. C. Chae, U. Waghmare, J. H. Lee, *Science* **2020**, *369*, 1343.
[5] T. Mikolajick, S. Slesazeck, M. H. Park, U. Schroeder, *MRS Bull.* **2018**, *43*, 340.
[6] M. Ghatge, G. Walters, T. Nishida, R. Tabrizian, *Nat. Electron.* **2019**, *2*, 506.
[7] H. Y. Yoong, H. Wu, J. Zhao, H. Wang, R. Guo, J. Xiao, B. Zhang, P. Yang, S. J. Pennycook, N. Deng, X. Yan, J. Chen, *Adv. Funct. Mater.* **2018**, *28*, 1806037.
[8] B. Max, M. Hoffmann, H. Mulaosmanovic, S. Slesazeck, T. Mikolajick, *ACS Appl. Electron. Mater.* **2020**, *2*, 4023.
[9] L. W. Martin, A. M. Rappe, *Nat. Rev. Mater.* **2016**, *2*, 16087.
[10] T. D. Huan, V. Sharma, G. A. Rossetti, R. Ramprasad, *Phys. Rev. B* **2014**, *90*, 064111.
[11] R. Materlik, C. Künneth, A. Kersch, *J. Appl. Phys.* **2015**, *117*, 134109.
[12] Y. Wei, P. Nukala, M. Salverda, S. Matzen, H. J. Zhao, J. Momand, A. S. Everhardt, G. Agnus, G. R. Blake, P. Lecoeur, B. J. Kooi, J. Íñiguez, B. Dkhil, B. Noheda, *Nat. Mater.* **2018**, *17*, 1095.

© 2022 Wiley-VCH GmbH

[13] Y. Qi, S. Singh, C. Lau, F.-T. Huang, X. Xu, F. J. Walker, C. H. Ahn, S.-W. Cheong, K. M. Rabe, *Phys. Rev. Lett.* **2020**, *125*, 257603.
[14] J. Müller, T. S. Böscke, U. Schröder, S. Mueller, D. Bräuhaus, U. Böttger, L. Frey, T. Mikolajick, *Nano Lett.* **2012**, *12*, 4318.
[15] T. Shiraishi, K. Katayama, T. Yokouchi, T. Shimizu, T. Oikawa, O. Sakata, H. Uchida, Y. Imai, T. Kiguchi, T. J. Konno, H. Funakubo, *Appl. Phys. Lett.* **2016**, *108*, 262904.
[16] R. Batra, T. D. Huan, J. L. Jones, G. Rossetti, R. Ramprasad, *J. Phys. Chem. C* **2017**, *121*, 4139.
[17] S. Liu, B. M. Hanrahan, *Phys. Rev. Mater.* **2019**, *3*, 054404.
[18] U. Schroeder, E. Yurchuk, J. Müller, D. Martin, T. Schenk, P. Polakowski, C. Adelmann, M. I. Popovici, S. V. Kalinin, T. Mikolajick, *Jpn. J. Appl. Phys.* **2014**, *53*, 08LE02.
[19] S. Starschich, U. Boettger, *J. Mater. Chem. C* **2017**, *5*, 333.
[20] M. D. Glinchuk, A. N. Morozovska, A. Lukowiak, W. Stręk, M. V. Silibin, D. V. Karpinsky, Y. Kim, S. V. Kalinin, *J. Alloys Compd.* **2020**, *830*, 153628.
[21] M. Hoffmann, U. Schroeder, T. Schenk, T. Shimizu, H. Funakubo, O. Sakata, D. Pohl, M. Drescher, C. Adelmann, R. Materlik, A. Kersch, T. Mikolajick, *J. Appl. Phys.* **2015**, *118*, 072006.
[22] M. H. Park, Y. H. Lee, H. J. Kim, T. Schenk, W. Lee, K. D.o Kim, F. P. G. Fengler, T. Mikolajick, U. Schroeder, C. S. Hwang, *Nanoscale* **2017**, *9*, 9973.
[23] X. Xu, F.-T. Huang, Y. Qi, S. Singh, K. M. Rabe, D. Obeysekera, J. Yang, M.-W. Chu, S.-W. Cheong, *Nat. Mater.* **2021**, *20*, 826.
[24] E. D. Grimley, T. Schenk, T. Mikolajick, U. Schroeder, J. M. Lebeau, *Adv. Mater. Interfaces* **2018**, *5*, 1701258.
[25] P. Nukala, M. Ahmadi, Y. Wei, S. De Graaf, E. Stylianidis, T. Chakrabortty, S. Matzen, H. W. Zandbergen, A. Björling, D. Mannix, D. Carbone, B. Kooi, B. Noheda, *Science* **2021**, *372*, 630.
[26] M. Lederer, T. Kämpfe, R. Olivo, D. Lehninger, C. Mart, S. Kirbach, T. Ali, P. Polakowski, L. Roy, K. Seidel, *Appl. Phys. Lett.* **2019**, *115*, 222902.
[27] S.-J. Chang, C.-Y.u Teng, Y.i-J. Lin, T.-M.u Wu, M.-H. Lee, B.i-H. Lin, M.-T. Tang, T.-S. Wu, C. Hu, E. Y.-T. Tang, Y.-C. Tseng, *ACS Appl. Mater. Interfaces* **2021**, *13*, 29212.
[28] G. Dong, S. Li, M. Yao, Z. Zhou, Y.-Q. Zhang, X.u Han, Z. Luo, J. Yao, B. Peng, Z. Hu, H. Huang, T. Jia, J. Li, W. Ren, Z.-G. Ye, X. Ding, J. Sun, C.e-W. Nan, L.-Q. Chen, J.u Li, M. Liu, *Science* **2019**, *366*, 475.
[29] D. Ji, S. Cai, T. R. Paudel, H. Sun, C. Zhang, L.u Han, Y. Wei, Y. Zang, M. Gu, Y.i Zhang, W. Gao, H. Huyan, W. Guo, D.i Wu, Z. Gu, E. Y. Tsymbal, P. Wang, Y. Nie, X. Pan, *Nature* **2019**, *570*, 87.
[30] S. S. Hong, M. Gu, M. Verma, V. Harbola, B. Y. Wang, D.i Lu, A. Vailionis, Y. Hikita, R. Pentcheva, J. M. Rondinelli, H. Y. Hwang, *Science* **2020**, *368*, 71.
[31] H. S. Kum, H. Lee, S. Kim, S. Lindemann, W. Kong, K. Qiao, P. Chen, J. Irwin, J. H. Lee, S. Xie, S. Subramanian, J. Shim, S.-H. Bae, C. Choi, L. Ranno, S. Seo, S. Lee, J. Bauer, H. Li, K. Lee, J. A. Robinson, C. A. Ross, D. G. Schlom, M. S. Rzchowski, C.-B. Eom, J. Kim, *Nature* **2020**, *578*, 75.
[32] R. Xu, J. Huang, E. S. Barnard, S. S. Hong, P. Singh, E.d K. Wong, T. Jansen, V. Harbola, J. Xiao, B. Y. Wang, S. Crossley, D.i Lu, S. Liu, H. Y. Hwang, *Nat. Commun.* **2020**, *11*, 3141.
[33] M. Hyuk Park, H. Joon Kim, Y.u Jin Kim, W. Lee, T. Moon, C. Seong Hwang, *Appl. Phys. Lett.* **2013**, *102*, 242905.
[34] P. Nukala, M. Ahmadi, J. Antoja-Lleonart, S. D.e Graaf, Y. Wei, H. W. Zandbergen, B. J. Kooi, B. Noheda, *Appl. Phys. Lett.* **2021**, *118*, 062901.
[35] T. Kiguchi, T. Shiraishi, T. Shimizu, H. Funakubo, T. J. Konno, *Jpn. J. Appl. Phys.* **2018**, *57*, 11UF16.
[36] T. Shimizu, T. Mimura, T. Kiguchi, T. Shiraishi, T. Konno, Y. Katsuya, O. Sakata, H. Funakubo, *Appl. Phys. Lett.* **2018**, *113*, 212901.
[37] S. S. Fields, S. W. Smith, P. J. Ryan, S. T. Jaszewski, I. A. Brummel, A. Salanova, G. Esteves, S. L. Wolfley, M. D. Henry, P. S. Davids, J. F. Ihlefeld, *ACS Appl. Mater. Interfaces* **2020**, *12*, 26577.
[38] A. I. Khan, A. Keshavarzi, S. Datta, *Nat. Electron.* **2020**, *3*, 588.
[39] J. Cao, S. Shi, Y. Zhu, J. Chen, *Phys. Status Solidi RRL* **2021**, *15*, 2100025.
[40] S. Estandía, N. Dix, J. Gazquez, I. Fina, J. Lyu, M. F. Chisholm, J. Fontcuberta, F. Sánchez, *ACS Appl. Electron. Mater.* **2019**, *1*, 1449.
[41] J. S. Heo, J. Eom, Y.-H. Kim, S. K. Park, *Small* **2018**, *14*, 1703034.
[42] W.-Y. Liu, J.-J. Liao, J. Jiang, Y.i-C. Zhou, Q. Chen, S.-T. Mo, Q. Yang, Q.-X. Peng, L.i-M. Jiang, *J. Mater. Chem. C* **2020**, *8*, 3878.
[43] H. Liu, T. Lu, Y. Li, Z. Ju, R. Zhao, J. Li, M. Shao, H. Zhang, R. Liang, X. R. Wang, R. Guo, J. Chen, Y.i Yang, T.-L. Ren, *Adv. Sci.* **2020**, *7*, 2001266.
[44] W. Xiao, C. Liu, Y. Peng, S. Zheng, Q. Feng, C. Zhang, J. Zhang, Y. Hao, M. Liao, Y. Zhou, *ACS Appl. Electron. Mater.* **2019**, *1*, 919.
[45] Y. Chen, Y. Yang, P. Yuan, P. Jiang, Y. Wang, Y. Xu, S. Lv, Y. Ding, Z. Dang, Z. Gao, T. Gong, Y. Wang, Q. Luo, *Nano Res.* **2022**, *15*, 2913.
[46] J. Lyu, I. Fina, R. Solanas, J. Fontcuberta, F. Sánchez, *ACS Appl. Electron. Mater.* **2019**, *1*, 220.
[47] S.u-T. Han, Y.e Zhou, V. A. L. Roy, *Adv. Mater.* **2013**, *25*, 5425.
[48] F. Liu, L.u You, K. L. Seyler, X. Li, P. Yu, J. Lin, X. Wang, J. Zhou, H. Wang, H. He, S. T. Pantelides, W.u Zhou, P. Sharma, X. Xu, P. M. Ajayan, J. Wang, Z. Liu, *Nat. Commun.* **2016**, *7*, 12357.
[49] W. Ding, J. Zhu, Z. Wang, Y. Gao, D.i Xiao, Y.i Gu, Z. Zhang, W. Zhu, *Nat. Commun.* **2017**, *8*, 14956.
[50] D. Pesquera, E. Khestanova, M. Ghidini, S. Zhang, A. P. Rooney, F. Maccherozzi, P. Riego, S. Farokhipoor, J. Kim, X. Moya, M. E. Vickers, N. A. Stelmashenko, S. J. Haigh, S. S. Dhesi, N. D. Mathur, *Nat. Commun.* **2020**, *11*, 3190.
[51] K.e Gu, T. Katayama, S. Yasui, A. Chikamatsu, S. Yasuhara, M. Itoh, T. Hasegawa, *Adv. Funct. Mater.* **2020**, *30*, 2001236.
[52] Z. Guan, H.e Hu, X. Shen, P. Xiang, N.i Zhong, J. Chu, C. Duan, *Adv. Electron. Mater.* **2020**, *6*, 1900818.
[53] N. Hansen, *Scr. Mater.* **2004**, *51*, 801.

© 2022 Wiley-VCH GmbH